Cement and Concrete Research 83 (2016) 188–202

Contents lists available at ScienceDirect

Cement and Concrete Research

journal homepage: www.elsevier.com/locate/cemconres

Micromechanical multiscale fracture model for compressive strength of blended cement pastes

Michal Hlobil [a,b,*], Vít Šmilauer [a], Gilles Chanvillard [c,1]

[a] Department of Mechanics, Faculty of Civil Engineering, CTU in Prague, Thákurova 7, 166 29 Prague 6, Czech Republic
[b] Institute for Mechanics of Materials and Structures (IMWS), Vienna University of Technology (TU Wien), Karlsplatz 13/202, A-1040 Wien, Austria
[c] Lafarge Centre de Recherche, 95 Rue du Montmurier, 38290 Saint-Quentin Fallavier, France

ARTICLE INFO

Article history:
Received 19 June 2015
Accepted 8 December 2015
Available online 9 March 2016

Keywords:
Compressive strength (C)
Calcium-Silicate-Hydrate (C-S-H) (B)
Microstructure (B)
Cement paste (D)
Blended cement (D)

ABSTRACT

The evolution of compressive strength belongs to the most fundamental properties of cement paste. Driven by an increasing demand for clinker substitution, the paper presents a new four-level micromechanical model for the prediction of compressive strength of blended cement pastes. The model assumes that the paste compressive strength is governed by apparent tensile strength of the C-S-H globule. The multiscale model takes into account the volume fractions of relevant chemical phases and encompasses a spatial gradient of C-S-H between individual grains. The presence of capillary pores, the C-S-H spatial gradient, clinker minerals, SCMs, other hydration products, and air further decrease compressive strength. Calibration on 95 experimental compressive strength values shows that the apparent tensile strength of the C-S-H globule yields approx. 320 MPa. Sensitivity analysis reveals that the "C-S-H/space" ratio, followed by entrapped or entrained air and the spatial gradient of C-S-H, have the largest influence on compressive strength.

1. Introduction

Compressive strength of concrete and its evolution belong to the most important and tested parameters. Due to the multiscale nature of concrete spanning the range from sub-nanometers to meters and its composite nature, several factors on different scales play a role in concrete compressive strength [1]. The most relevant initial factors include the binder type, aggregate type, extent of the interfacial transition zone, and the air content. Time-dependent factors play a role mainly in binder's reaction kinetics which is reflected in the evolution of chemical phases with a direct impact on stiffness and strength evolution.

Up to the time of Hoover Dam construction in the 1930s, a cementitious binder was mostly equivalent to Portland cement. Since that time, Portland clinker has been substituted more and more by supplementary cementitious materials such as slag, fly ash, limestone or silica fume. The substitution rose from 17% in 1990 to 25% in 2010 among the top world cement producers [2]. A further shift is expected, motivated by economical, ecological and sustainable benefits [3,4].

The question on the origin of concrete strength becomes reinitiated with the advent of blended binders. The famous Powers' empirical relationship between the gel-space ratio and compressive strength developed for Portland-based materials needs several adjustments when dealing with blended binders [5]. The main reason lies in altered chemistry where a chemically heterogeneous gel differs in chemical phases, e.g. CH may be depleted in pozzolanic reactions or C-A-H phases may emerge. To overcome these deficiencies, micromechanical models taking into account volume fractions directly have been set up for more fundamental understanding.

Continuum micromechanical models able to reproduce the evolution of stiffness and compressive strength have recently been published, e.g. for Portland-based materials [6,7] or for cocciopesto mortars [8]. Pichler et al. [9] used spherical and acicular representation of hydrates to capture percolation threshold during hydration and the onset on elasticity and strength. Hydrates consisted of solid C-S-H, small and large gel pores and other hydration products. The strength criterion was based on deviatoric strength of hydrates which was identified to be 69.9 MPa. Once the quadratic stress average in arbitrarily oriented needle-shaped hydrates exceeded this strength, the material failed in a brittle manner. Similar modeling approach was also used for C_3S, C_2S, $C_3S + C_3A +$ gypsum pastes, assuming that only C-S-H with the Mohr–Coulomb quasi-brittle failure criterion was responsible for the compressive strength of pastes [10]. Computational micromechanical models generally allow taking into account nonlinear elasto-plasto-damage constitutive laws at the expense of computational time. Several 2D and 3D lattice and continuum models were applied for cement paste [11] or concrete [12,13,14] to mention a few.

In this paper, a new four-level micromechanical fracture model for blended cement pastes is presented, starting from C-S-H globule up to cement paste with entrapped/entrained air. The lowest homogenization

* Corresponding author.
E-mail address: michal.hlobil@fsv.cvut.cz (M. Hlobil).
[1] Gilles Chanvillard (21.1.1963 - 24.10.2015) passed away very unexpectedly during the revision process of this paper.

http://dx.doi.org/10.1016/j.cemconres.2015.12.003
0008-8846/

level contains C-S-H globules, small and large gel pores [15]. A C-S-H globule is considered to be the only strain-softening component in the multiscale model, leading essentially to failure at each level. Softening occurs under excessive tension or compression described by an elasto-damage constitutive law introduced in Section 2.1. Higher levels also use the elasto-damage constitutive law for a phase containing C-S-H globules with an updated homogenized stiffness, strength, and estimated fracture energy. Hence, the strength of cement paste origins from the softening and failure of C-S-H globule. The multiscale model accounts for volume fractions of C-S-H, other hydrates, capillary porosity, clinker, supplementary cementitious materials, entrained/entrapped air and considers the spatial gradient of C-S-H among clinker grains.

The model contains two independent variables that need to be calibrated from experimental data: the apparent tensile strength of C-S-H globules and the spatial gradient of C-S-H. Numerical results for elastic modulus and compressive/tensile strength on each scale are further fitted to microstructure-calibrated analytical expressions, speeding up the whole validation part. Sensitivity analysis identifies key components for the compressive strength of blended pastes.

2. Finite element analysis

2.1. Fracture material model and its implementation

The nonlinear constitutive behavior of quasi-brittle materials, such as cement paste, mortar or concrete, can be generally described by three common theories: plasticity, fracture mechanics, damage mechanics, or their combinations. Plasticity fails to describe stiffness degradation which is needed for strain softening, strain localization, and the size effect, although several extensions were proposed [16]. Linear elastic fracture mechanics can only deal with brittle materials with a negligible process zone ahead of a crack tip and cannot handle microcrack nucleation into a macrocrack. Damage mechanics, particularly the cohesive crack model, defines the traction–separation law in a plastic zone of an opening crack which is related to the fracture energy of a material and stiffness degradation. This nonlinear fracture mechanics approach offers reasonable stress–strain predictions with minimum parameters, reasonable computation time, and captures the size effect of quasibrittle materials [17]. More elaborated plastic-damage models have been successfully used for the mesoscale analysis of concrete [14].

The present material model is based on fracture mechanics on all considered four scales. A crack starts to grow when cohesive stress is exceeded anywhere in the material. For uniaxial tension of a homogeneous material, this cohesive stress corresponds obviously to the tensile strength, f_t. Damage mechanics uses the concept of the equivalent strain, $\tilde{\varepsilon}$, as a descriptor of damage evolution. Damage becomes initiated when the equivalent strain, $\tilde{\varepsilon}$, exceeds strain at the onset of cracking, $\varepsilon_0 = f_t/E$, where E is the elastic modulus. The Rankine criterion for tensile failure defines $\tilde{\varepsilon}$ as

$$\tilde{\varepsilon} = \frac{\sigma_1}{E}, \sigma_1 > 0 \tag{1}$$

where σ_1 is the maximum positive effective principal stress on undamaged-like material, see Fig. 1 (a).

Under uniaxial compressive stress, crack initiation occurs under a different mechanism. A homogeneous material experiences only one negative principal stress and the deviatoric stress. Cracking in diagonal, shear band zone is often encountered on cementitious specimens, however, the physical mechanism is again tensile microcracking in voids and defects of the underlying microstructure [pp 297, 17]. Such a behavior has already been described in the work of Griffith [18], and McClintock and Walsh [19], and we briefly review this theory and extend it with an equivalent strain to be used in the framework of damage mechanics.

It is assumed that a material contains randomly oriented 2D elliptical flat voids with various aspect ratios $m = b/a$, see Fig. 1 (b). Further notations assume that tensile stress is positive and $\sigma_1 \geq \sigma_3$. The voids have a negligible area and only represent stress concentrators and internal defects in a material. Under macroscopic biaxial stress, the maximum tensile stress among all voids, $m \cdot \sigma_\eta$, appears on a critically inclined elliptical void under a critical angle ψ

$$\cos 2\psi = \frac{\sigma_3 - \sigma_1}{2(\sigma_3 + \sigma_1)}, \frac{\sigma_1}{\sigma_3} \geq -\frac{1}{3} \tag{2}$$

$$m \cdot \sigma_\eta = \frac{-(\sigma_1 - \sigma_3)^2}{4(\sigma_1 + \sigma_3)} \tag{3}$$

Crack formation occurs when the tangential tensile stress, $m \cdot \sigma_\eta$, equals to the tensile strength of the matrix. Since σ_η and the crack geometry, m, cannot be measured directly, it is reasonable to relate their product to the uniaxial macroscopic tensile stress, $\bar{\sigma}_1$, as proposed by Griffith [18]

$$\bar{\sigma}_1 = \frac{m \cdot \sigma_\eta}{2} \tag{4}$$

The material starts to crack when $\bar{\sigma}_1$ equals to the uniaxial macroscopic tensile strength f_t. Note that the tensile strength of the

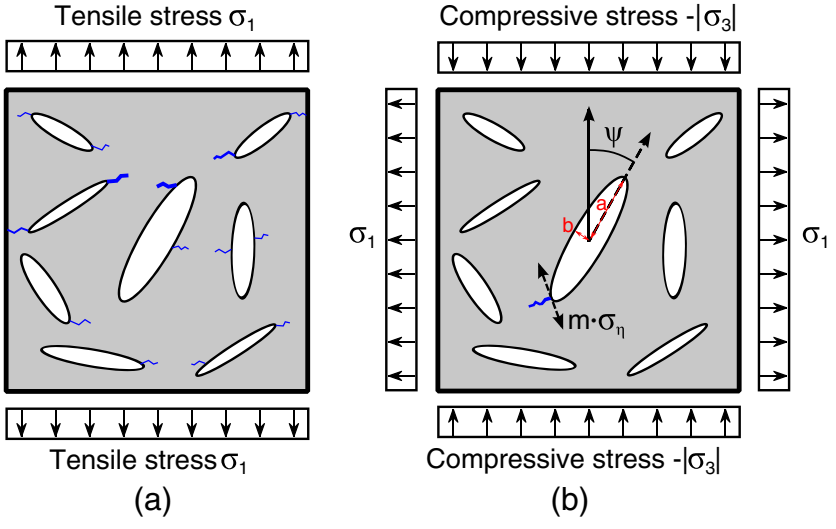

Fig. 1. Crack evolution during (a) uniaxial tensile stress and (b) compressive stresses. The material contains randomly oriented elliptical voids with negligible area.

homogeneous matrix (intrinsic strength) and the crack geometry remain unknown separately and we can assess only apparent macroscopic tensile strength f_t. Plugging Eq. (3) into Eq. (4) and further into Eq. (1) leads to the definition of the equivalent strain, $\tilde{\varepsilon}$, under compression-dominant loading

$$\tilde{\varepsilon} = \frac{1}{E} \cdot \frac{-(\sigma_1 - \sigma_3)^2}{8(\sigma_1 + \sigma_3)} \tag{5}$$

An interesting feature of the Griffith model is that the ratio of the uniaxial compressive-to-tensile strength equals to 8

$$|f_c| = 8 f_t \tag{6}$$

This can be verified when plugging $\sigma_1 = f_t$ into Eq. (1) which leads to $\tilde{\varepsilon} = f_t/E$. Plugging $\sigma_1 = 0, \sigma_3 = -8 f_t$ into Eq. (5) leads to the same equivalent strain.

Since the equivalent strain may arise from the Rankine of Griffith criterion, it is necessary to compare both Eqs. (1) and (5) and to select the higher equivalent strain. Linear softening is assumed in the simulations. The softening shape has a little effect on the computed macroscopic strength which is the main objective of this paper and naturally affects the post-peak behavior. The linear cohesive law takes the form

$$\sigma = f_t \left(1 - \frac{\omega}{\omega_f}\right) \tag{7}$$

where w is a crack opening and w_f is the maximum crack opening at zero stress. According to the formulation of the isotropic damage model, the uniaxial tensile stress obeys the law

$$\sigma = (1 - \omega) E \tilde{\varepsilon} \tag{8}$$

Let us consider the fracture energy in mode I, G_f, and the effective thickness of a crack band h, which corresponds to the finite element size in the direction of the maximum principal strain [17]. This ensures objective results, independent on finite element size [20]. Notice that $w = h\omega\tilde{\varepsilon}$ and $w_f = 2G_f/f_t$. The evolution of isotropic damage is obtained by combining Eqs. (7) and (8)

$$\omega = \left(1 - \frac{\varepsilon_0}{\tilde{\varepsilon}}\right)\left(1 - \frac{hE\varepsilon_0^2}{2G_f}\right)^{-1} \tag{9}$$

The performance of the proposed Griffith–Rankine model under the plane stress condition is demonstrated in Fig. 2 for the onset of cracking. The Mohr-Coulomb model gives similar results for the friction angle of 51.1° and $c_0/f_t = \sqrt{2}$, which keeps the compressive/tensile strength ratio of 8. The differences in both models are small but the Griffith–Rankine model provides in addition the equivalent strain which is used for damage quantification.

The Griffith–Rankine model was implemented in OOFEM package [21]. The basic test covered a uniaxially loaded one brick element under pure tension or compression for $E = 20$ GPa, $G_f = 20$ J/m^2, $f_t = 5$ MPa and the element size $10 \times 10 \times 10$ mm. Fig. 3 shows the response in terms of average stress and strain over the element. Note that the linear softening law defined in the integration point may be distorted on the element scale since damage occurs in more integration points and later becomes localized into one integration point. The material model provides fracture energy in compression, which is theoretically 64 times larger than that in tension. However, such fracture energy in compression is a fictitious value since other mechanisms for energy dissipation occur such as buckling within the microstructure [22].

To demonstrate further the performance of the Griffith–Rankine model, Fig. 4 shows the strain localization in shear bands under the uniaxial compression test under plane stress condition. A layer of finite elements with steel properties is attached to the top and bottom which restrains the horizontal displacement and induces the horizontal shear stress in the contact. This mimics the situation of the standard uniaxial compression test without teflon pads. Material properties remain the same as in the previous case and the microstructure size 20×20 mm is discretized to 20×20 finite elements. Black lines show crack orientation in damaged parts.

2.2. Boundary conditions and intrinsic properties

The four-level multiscale model utilizes a 2D or 3D finite element analysis on each scale, where the Griffith-Rankine constitutive laws govern the crack growth and material softening. The discretization of the microstructure relies on the length scale considered. Each scale contains relevant chemical phases in correct volume proportions.

The prescribed boundary conditions on a unit cell (UC) reflect uniaxial loading on each scale. Periodic boundary conditions would provide the most reliable estimation of elastic properties when cement paste is considered as a whole at one homogenization level, without any hierarchical approach [23]. However, kinematic boundary conditions in the top and bottom UC's surfaces yield a better match for this hierarchical approach for the elastic modulus. The UC is loaded by eigenstrain increment in the vertical direction which builds up the uniaxial macroscopic compressive stress.

Table 1 summarizes intrinsic elastic and apparent fracture properties assigned to relevant phases during simulations. While nanoindentation previously quantified elastic properties [24], the tensile strengths of C-S-H and C-S-H globules need to be estimated by means of downscaling from experimental data on cement pastes, see Section 4.6.

The fracture energy of individual components with their interfaces is estimated, based on available data. For example, the C-S-H–C-S-H debonding energy was computed to lay between 0.38 and

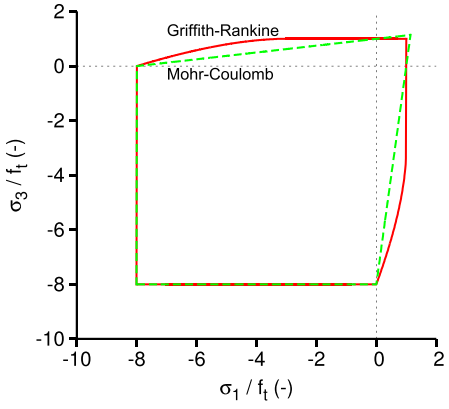

Fig. 2. Surface at the onset of cracking according to two models under the plane stress condition.

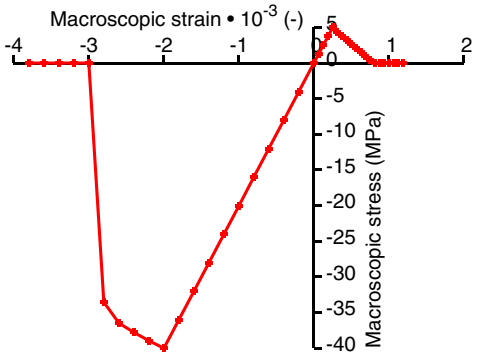

Fig. 3. Test of one linear brick element under uniaxial tension/compression with 8 integration points.

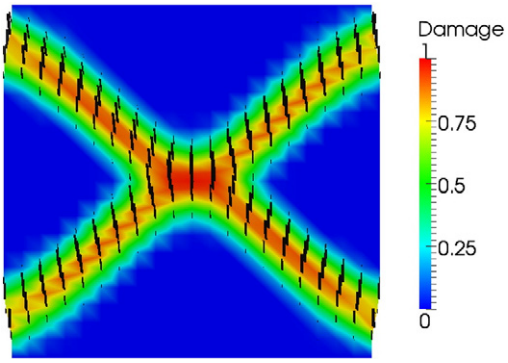

Fig. 4. Strain localization in shear bands under the uniaxial compression test under plane stress. 20×20 quadrilateral elements (20×20 mm), deformation exaggerated 40×, damage showed for the end of softening.

2.85 J/m^2[25]. However, this energy is too low and the pull-out mechanism of CH crystals increases this energy to a theoretical range of 7.55–283 J/m^2, which is more realistic with measured values of fracture energy of cement pastes [25]. Molecular dynamics simulations performed on atomic scale yield fracture energy of C-S-H as 1.72 ± 0.29 J/m^2 [26]. The value of fracture energy is not very sensitive parameter for the peak stress of a material, see Fig. 29, but rather influences post-peak behaviour which is not the primary focus of this paper.

3. Multiscale model for cement pastes

The previous success of the gel-space descriptor coined by Powers indicates that strength emerges mainly on submicrometer resolution [7,30].

A four-level hierarchical model for cement paste, see Fig. 5, is constructed to account for major and minor effects influencing strength. The coupling between levels occurs through upscaling the elastic modulus, E, and the tensile strength, f_t. The tensile strength on each level is identified from compressive strength, f_c, using the Griffith criterion, which yields a constant ratio $f_c/f_t = 8$, see Section 2.1. The fracture energy, G_f, is not directly upscaled, instead, it is explicitly defined at each level, see further discussion in Section 4.13.

Level 0: C-S-H considers C-S-H globules packing to densities between C-S-H$_{LD}$ and C-S-H$_{HD}$. Together with Jennings [15], the C-S-H globule consists of calcium silicate sheets, interlayer space, intraglobule space, and monolayer water. The globules become mixed with small and large gel pores ($1\ \text{nm} < d < 12\ \text{nm}$). The characteristic size spans the range of 1 - 100 nm.

Level 1: C-S-H foam contains C-S-H together with capillary porosity. To mimic an uneven distribution of C-S-H among grains in cement paste, C-S-H have a spatial gradient. The characteristic size spans the range of 100 nm - 10 μm.

Level 2: Cement paste adds unhydrated clinker and all remaining hydration products (CH, AFm, AFt,...) inside the homogenized C-S-H foam. The characteristic size spans the range of 10 - 100 μm.

Level 3: Cement paste with air captures entrained or entrapped air, decreasing the resulting mechanical properties. The characteristic size spans the range of 100 - 1000 μm.

C-S-H foam in Level 1 covers a region between individual clinker grains. The size of the region depends on (i) the mean size of clinker grains, and on (ii) the initial composition of cement paste specified by the water-to-binder mass ratio. In modeling, such microstructure was simplified by assigning a constant UC height of 10 μm.

It is worthy to mention that C-S-H is not a true gel but a precipitate, signalized by the presence of capillary porosity, by a more-or-less constant gel porosity during the C-S-H formation, and by the C-S-H appearance mainly around cement clinker grains [31] which can be observed in SEM/BSE images. To investigate the spatial distribution of C-S-H between grains, μCT scans of cement pastes from The Visible Cement Dataset created by NIST were used [32]. Two different cement pastes were considered with water/cement ratio equal to 0.3 and 0.45, both produced from a reference cement #133. Cement paste with w/c = 0.3 was investigated at 8 and 162 h after mixing whereas cement paste with w/c = 0.45 was studied at 8 and 124 h. All μCT scans were sliced to create 2D images, thresholded to separate clinker, hydrates and capillary pores based on known volume fractions. In this particular case, C-S-H corresponded to hydrates. Fig. 6 shows the calculated two-point correlation function between hydrates (C-S-H) and the closest grain surface. Thresholded images of pastes tested 8 hours after casting show that C-S-H precipitate mainly around cement grains for both w/c ratios studied. Older pastes exhibit a denser microstructure but a larger w/c ratio (here w/c = 0.45) indicates a higher gradient of C-S-H.

A common assumption of hydration models is concentric growth of spherical shells representing hydration products around original grains such as HYMOSTRUC [33,34] or μic [35,36]. In the proposed multiscale model we approximate the spatial gradient of the C-S-H distribution by a spatial density function ρ as

$$\rho(x,\beta) = \frac{1}{\beta}\exp\left(-\frac{x/\ell_{UC}}{\beta}\right) \tag{10}$$

where x stands for the distance from the clinker grain surface, β is a parameter of the exponential distribution and ℓ_{UC} is the characteristic length of UC. Low values of β indicate a high gradient of C-S-H in space. Fig. 7 illustrates the impact of β on the C-S-H distribution at the level of C-S-H foam.

The term "gel" coined by Powers described a mixture of amorphous C-S-H and all other crystalline hydration products [30]. However, recent detailed modeling of C_3S and C_2S pastes revealed that not all hydration products contribute to the compressive strength equally [10]. In fact, more precise results for the compressive strength prediction were

Table 1
Intrinsic elastic and apparent fracture properties of relevant chemical phases considered in the multiscale hierarchical simulation.

	Elastic modulus (GPa)	Poisson's ratio (−)	Tensile (compressive) strength (MPa)	Fracture energy (J/m^2)	Ref.
C-S-H globule	57.1	0.27	320 (2560)	2[a]	[10]
C-S-H$_{LD}$	21.7	0.24	66 (528)[b]	5[a]	[27]
C-S-H$_{HD}$	29.4	0.24	107 (856)[b]	5[a]	[27]
Water-filled porosity	0.001	0.499924	–	–	[23]
CH	38.0	0.305	–	–	[27]
AFt	22.4	0.25	–	–	[28]
AFm	42.3	0.324	–	–	[28]
Clinker minerals	139.9	0.30	–	–	[7]
Mature cement paste	–	–	–	15	[29]

[a]) Higher fracture energy leads to the same material strength.
[b]) Calculated from packing of C-S-H globules.

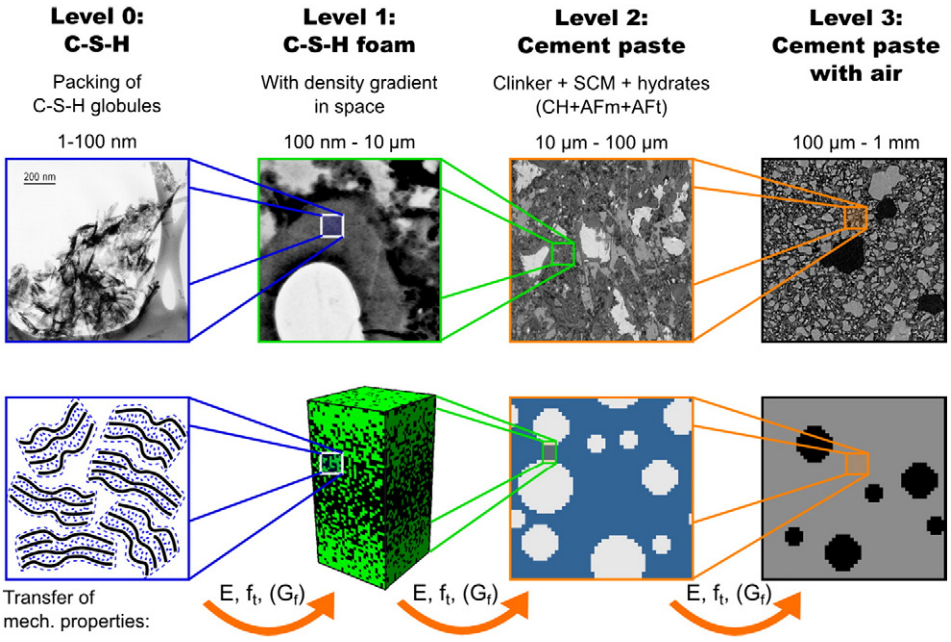

Fig. 5. Four-level hierarchical multiscale model. TEM/SEM images from left to right: Eric Lachowski, S.Y. Hong and F.P. Glasser (http://publish.illinois.edu/concretemicroscopylibrary/transmission-electron-microscopy-tem/); L. Kopecký (CTU in Prague); Paul Stutzman (NIST, http://publish.illinois.edu/concretemicroscopylibrary/magnification-progression-series-1000x/); D. P. Bentz, et al. (Visible Cement Dataset: http://visiblecement.nist.gov)

obtained when C-S-H was the only failing component in the cement paste. A similar conclusion is supported by Fig. 8 which shows the contribution of clinker minerals to the overall compressive strength of hydrated pastes [37]. While minerals producing C-S-H yield comparable results, C_3A generating AFt yields a much lower strength. In the presented multiscale model, C-S-H are considered as the weakest active binding phase, interconnecting other crystalline hydration products, unreacted clinker minerals, and SCMs. Instead of using the "gel/space ratio", we define the term "C-S-H/space ratio", γ_{CSH}, as

$$\gamma_{CSH} = \frac{\phi_{\mathrm{CSH}}}{\phi_{\mathrm{CSH}} + \phi_{cappor}} \tag{11}$$

where ϕ_{CSH} and ϕ_{cappor} stand for the volume fractions of C-S-H (including gel pores) and capillary porosity, respectively.

Level 2 of the multiscale model describes cement paste as a two-phase material. For the reason of simplicity, crystalline hydration products, clinker minerals, and SCMs are merged together into one fictitious isotropic elastic phase, see Fig. 5. Due to the crystalline morphology, a self-consistent scheme [38] is used to estimate the effective elastic property of this homogenized phase which is based on the volume fractions and elastic properties of individual microstructural constituents according to Table 1. The homogenized phase is then embedded into the C-S-H foam where it acts as solid inclusions.

Level 3 describes the effect of entrapped or entrained air inside the cement paste which has a pronounced impact on the mechanical properties. The microstructure on this level consists of circular voids which are embedded into a homogeneous cement paste.

4. Results and discussion

The four-level model aims to predict the elastic modulus and compressive/tensile strength of cement pastes by hierarchical homogenization. The tensile strength of the C-S-H globule plays the most important role since it is projected onto higher hierarchical levels. This strength value will be calibrated from macroscopic data since no direct experimental method is available today, see Section 4.6. The results from finite element simulations are approximated using analytical functions on all hierarchical levels to speed up the validation.

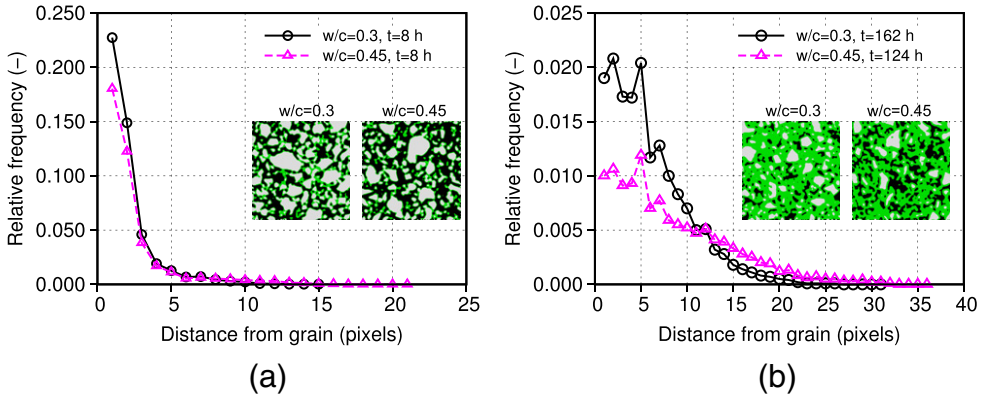

Fig. 6. Spatial distribution of C-S-H between grains for a) early-age pastes and b) for older pastes. One pixel corresponds to 0.95 μm.

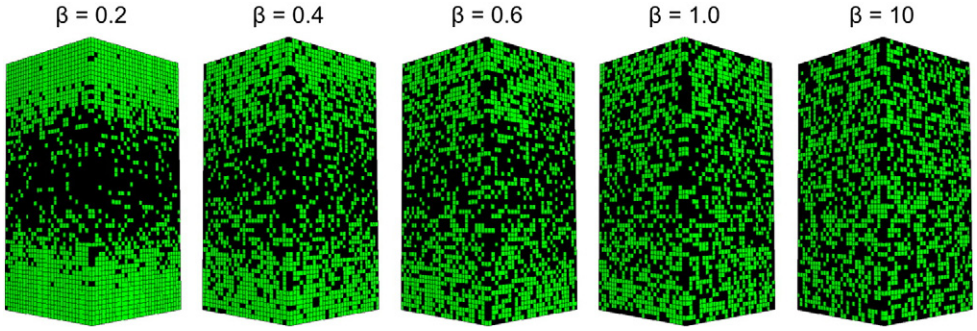

Fig. 7. The impact of the parameter β on the C-S-H distribution (Level 1) for C-S-H/space ratio $\gamma_{CSH}=0.7$, UC size $5\times5\times10$ μm.

4.1. Level 0: C-S-H

The presented level considers time-dependent and spatially uniform packing density of C-S-H globules as an approximation of a colloidal system of C-S-H gel. The shape of the globule is set as one voxel (5 nm), without specifying globule's orientation, see Fig. 10. The globule is treated as an isotropic material.

Jennings [39] coined two morphologies of C-S-H (low and high density) which emerge from different packing densities of C-S-H globules. Nanoindentation experiments carried out by Constantinides and Ulm [27] identified elastic properties of C-S-H, see Table 1, as well as derived limit packing densities as $\eta_{CSH_{LD}}=0.63$ and $\eta_{CSH_{HD}}=0.76$ [40]. A packing density of globules is estimated from the CEMHYD3D hydration model [41] with the implemented confinement algorithm [23] and it is a function of the initial water-to-binder mass ratio, w/b, and the time-dependent capillary porosity, ϕ_{cappor}. Fig. 9 shows the evolution for three w/b ratios with the approximation of volume fraction of C-S-H_{HD} within C-S-H as

$$\phi_{CSH_{HD}} = \left[1 + 5000\ \phi_{cappor}^{(2.5+5\ w/b)}\right]^{-1} \tag{12}$$

The confinement algorithm makes no difference between various solid phases, hence it captures both OPC and blended cements [23]. Depending on the volume fraction of C-S-H_{HD} within C-S-H, we interpolate the actual packing density of globules as

$$\eta_{glob} = \eta_{CSH_{LD}} + \left(\eta_{CSH_{HD}} - \eta_{CSH_{LD}}\right)\phi_{CSH_{HD}} = 0.63 + 0.13\ \phi_{CSH_{HD}} \tag{13}$$

Similarly, Young's modulus of C-S-H spans the range between $E_{CSH_{LD}}=21.7$ GPa and $E_{CSH_{HD}}=29.4$ GPa, see Table 1.

$$E^0_{CSH} = E_{CSH_{LD}} + \left(E_{CSH_{HD}} - E_{CSH_{LD}}\right)\phi_{CSH_{HD}} = 21.7 + 7.7\ \phi_{CSH_{HD}} \tag{14}$$

The apparent tensile strength of the globule governs strength at higher hierarchical levels. Section 4.6 shows that the globule's apparent tensile strength was identified as

$$f_{t,glob} = 320\ \text{MPa} \tag{15}$$

Fig. 10 shows UCs for C-S-H_{LD} and C-S-H_{HD} types used for finite element simulations. Fig. 11 displays the evolution of the C-S-H tensile strength depending on the packing density. The approximation reads

$$f^0_{t,CSH} = f_{t,glob}\exp\left(-1.101\ \frac{1-\eta_{glob}{}^{5.133}}{\eta_{glob}}\right) \tag{16}$$

which yields the apparent tensile strength of C-S-H_{LD} and C-S-H_{HD} as $f_{t^0,CSH_{LD}}=66$ MPa and $f_{t^0,CSH_{HD}}=107$ MPa, respectively. By extrapolation to globule packing density $\eta_{glob}=1$ we identify the apparent tensile strength of the globule as 320 MPa. The compressive strength of C-S-H can be obtained from the Griffith criterion in Eq. (6), which yields the apparent compressive strength $f_{c^0,CSH_{LD}}=528$ MPa, and $f_{c^0,CSH_{HD}}=856$ MPa.

4.2. Level 1: C-S-H foam

C-S-H precipitating in the region between individual clinker grains forms a spatial gradient, see Fig. 7. This level contains only C-S-H which is intermixed with capillary porosity. The computational UC is composed from a 3D uniform mesh, consisting of $20\times20\times40$ brick elements with linear displacement interpolations and with a resolution of 0.25 μm/voxel, yielding the UC size of $5\times5\times10$ μm. The proposed setup assumes that the top and bottom planes of UC touch the surfaces of clinker grains and C-S-H precipitates in between. C-S-H is generated randomly in UC but its spatial distribution follows Eq. (10). Fig. 12 shows the stress-strain diagram obtained from a FE model of C-S-H foam

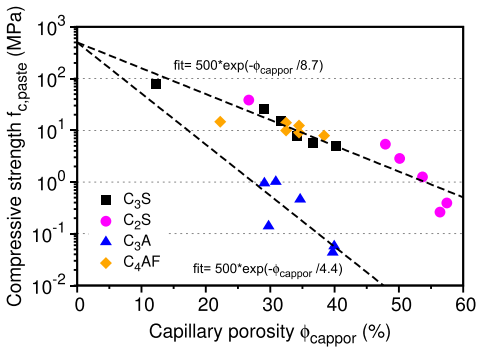

Fig. 8. Compressive strength of pastes with w/c = 0.45 measured on cylinders with a diameter of 12.7 mm and height of 25.4 mm [37].

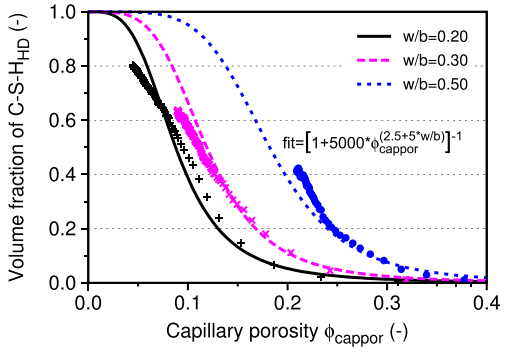

Fig. 9. Evolution of the volume fraction of C-S-H_{HD} within C-S-H as a function of capillary porosity and the initial composition from the CEMHYD3D model. C-S-H_{LD} always appear at the beginning of hydration.

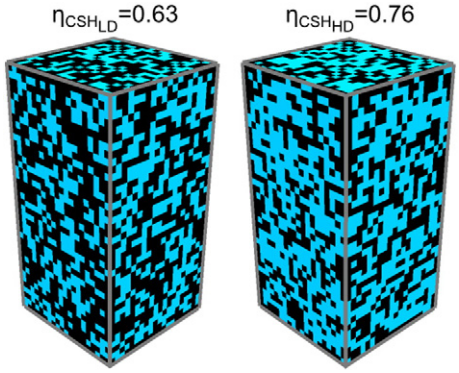

Fig. 10. UCs for C-S-H_{LD} and C-S-H_{HD}, 20×20×40 brick elements (UC size 100×100×200 nm).

consisting solely of C-S-H_{LD} using the C-S-H/space ratio $\gamma_{CSH}=0.7$, $\beta=0.6$, and $f^0_{t,CSH}=66$ MPa.

The results from numerical simulations on the level of C-S-H foam show that the spatial gradient has only a weak impact on elasticity. The elastic modulus for percolated microstructures linearly increases with the increasing C-S-H/space ratio, see Fig. 13. An analytical approximation to numerical results of the elastic modulus of C-S-H foam yields

$$E^I_{foam}=E^0_{CSH}\exp\left(A_1\frac{\gamma_{CSH}{}^{B_1}-1}{\gamma_{CSH}}\right) \tag{17}$$

$$A_1=0.820\exp\left(-4.949\frac{\beta^{0.02}-1}{\beta^{2.8}}\right),\beta\in\langle 0.4;1.0\rangle \tag{18}$$

$$B_1=1.818\exp\left(4.310\frac{\beta^{0.02}-1}{\beta^{2.8}}\right),\beta\in\langle 0.4;1.0\rangle \tag{19}$$

where $\beta\in\langle 0.4;1.0\rangle$. Higher β values are equivalent to a uniform distribution.

Compressive strength determined on identical microstructures exhibits a high sensitivity on the spatial gradient, see Fig. 14. This can be explained by the stress concentration in diluted areas which decrease the load-bearing capacity. The analytical approximation to numerical data results in more complicated equations, capturing the effect of the C-S-H/space ratio γ_{CSH} and the spatial gradient by means of the parameter β as

$$f^I_{c,foam}=f^0_{c,CSH}\exp\left(-C_1\frac{1-\gamma_{CSH}{}^{D_1}}{\gamma_{CSH}}\right) \tag{20}$$

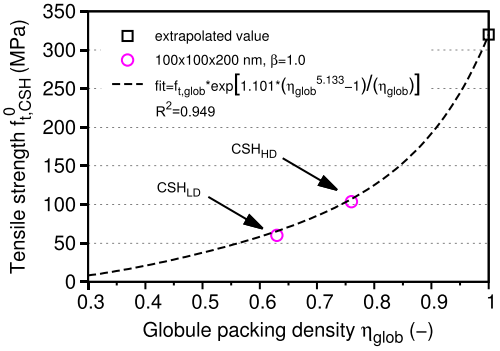

Fig. 11. Tensile strength of C-S-H depending on the globule packing density. Circles represent results from FE simulations on 20×20×40 brick elements (100×100×200 nm), $\beta=1.0$ and $G_f=2$ J/m^2.

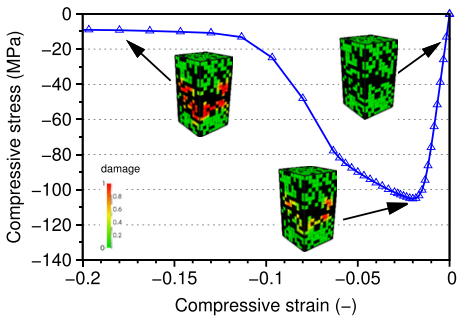

Fig. 12. Stress-strain diagram obtained on C-S-H foam using $\gamma_{CSH}=0.7$, $\beta=0.6$, and $f^0_{t,CSH}=66$ MPa.

$$C_1=1.101\exp\left(-0.296\frac{\beta-1}{\beta}\right),\beta\in\langle 0.4;1.0\rangle \tag{21}$$

$$D_1=-11.058\beta^{1.987}+16.191\beta,\beta\in\langle 0.4;1.0\rangle \tag{22}$$

4.3. Level 2: cement paste

Level 2 uses a 2D uniform mesh composed of 100×100 quadrilateral elements (UC size of 100×100 μm) with linear displacement interpolations. The comparison with 3D UC proved that 2D model under plane stress yields very similar results for elasticity and peak stress. The 2D model allows capturing larger and more detailed microstructures. The damage model was assigned to a homogeneous C-S-H foam. The actual size of inclusions follows a stepwise particle size distribution with circles of 5, 10, and 15 μm in diameter.

Introducing a solid inclusion into a homogeneous C-S-H foam results in an increase of the stiffness of the reinforced foam on the one hand, and in a decrease of the compressive strength on the other hand. Results from FE simulations show that the overall stiffness of cement paste proportionally increases with the quantity of inclusions as well as their stiffness, see Fig. 15.

An analytical approximation for elasticity prediction yields

$$E^{II}_{CP}=E^I_{foam}\left[1+\phi_{incl}\left(0.0102E_{incl}+0.278E^I_{foam}{}^{0.2}\right)\right] \tag{23}$$

The high stiffness contrast between solid inclusions and the C-S-H foam influences stress trajectories to concentrate between inclusions, resulting in a decrease of the nominal strength of cement paste, see

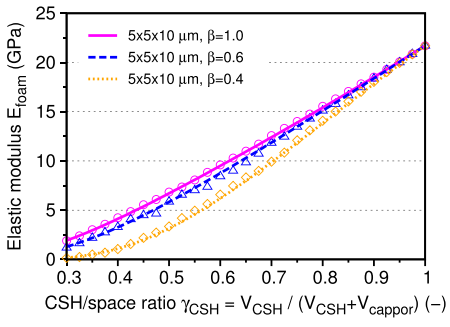

Fig. 13. Elastic modulus evolution for Level 1 (C-S-H foam), assuming solely C-S-H_{LD} with the globule packing density $\eta_{glob}=\eta_{CSH_{LD}}=0.63$. Points represent results from FE simulations on UC 20×20×40 brick elements (UC size 5×5×10 μm) and the lines are analytical approximations.

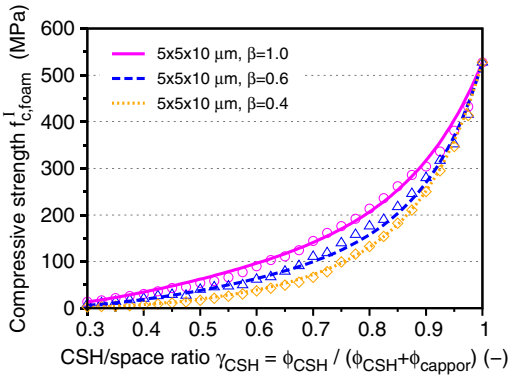

Fig. 14. Compressive strength evolution for Level 1 (C-S-H foam), assuming solely C-S-H_{LD} with the globule packing density $\eta_{glob} = \eta_{CSH_{LD}} = 0.63$ and the corresponding compressive strength $f_{c^0,CSH} = 528$ MPa. Points represent results from FE simulations on UC 20×20×40 brick elements (UC size 5×5×10 µm) and lines are analytical approximations.

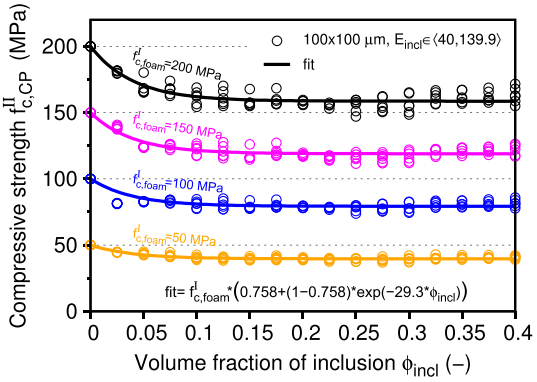

Fig. 16. Compressive strength evolution for level 2 (cement paste), assuming $f_{c^I,foam} = 50,100,150,200$ MPa. Circles represent results from FE simulations on a 2D microstructure on 100×100 quadrilateral elements (UC size 100×100 µm) for $f_{c^I,foam} = 50,100,150,200$ GPa with varying stiffness of the inclusion $E_{incl} = 40,50,60,70,105,139.9$ GPa.

Fig. 16. The impact of inclusion's stiffness on the resultant decrease of compressive strength is insignificant.

An analytical approximation for compressive strength prediction yields

$$f^{II}_{c,CP} = f^{I}_{c,foam}[0.758 + (1-0.758)\exp(-29.3\,\phi_{incl})] \tag{24}$$

4.4. Level 3: cement paste with air

Level 3 again uses a 2D uniform mesh composed of 50×50 quadrilateral elements (UC size 1000×1000 µm). To account for the random size of entrapped or entrained air bubbles in real cement pastes, the size of the bubbles follows a step-wise particle size distribution with spheres of 20, 60, and 100 µm in diameter.

The presence of air in the cement paste significantly reduces both observed mechanical properties. Fig. 17 shows the decrease of the elastic modulus with the increasing volume fraction of the air content ϕ_{air}. An analytical approximation for elasticity prediction reads

$$E^{III}_{CP+air} = E^{II}_{CP}(1-3\phi_{air}) \tag{25}$$

Every 1% of entrained (or entrapped) air results in a proportional decrease of the elastic modulus by 3%.

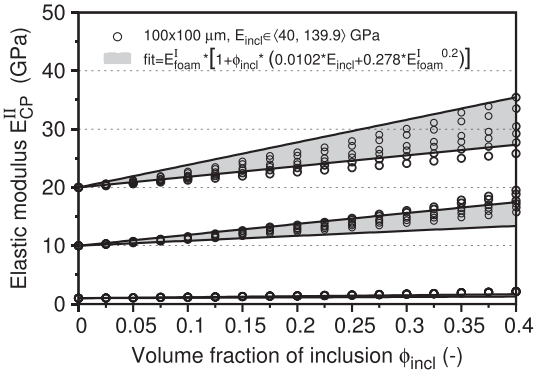

Fig. 15. Elastic modulus evolution for Level 2 (cement paste) assuming $E^{I}_{foam} = 1,10,20$ GPa. Circles represent results from FE simulations on a 2D microstructure on 100×100 quadrilateral elements (UC size 100×100 µm) with varying stiffness of the inclusion $E_{incl} = 40,50,60,70,105,139.9$ GPa .

Voids in a homogeneous matrix cause the concentration of stress, effectively reducing the compressive strength, see Fig. 18. An analytical approximation to numerical simulations reads

$$f^{III}_{c,CP+air} = \begin{cases} f^{II}_{c,CP} - 0.2\, f^{II}_{c,CP}\dfrac{\phi_{air}}{0.0025} & \text{for } \phi_{air} \le 0.0025 \\ 0.8\, f^{II}_{c,CP}\exp\left(\dfrac{-4.056\,(\phi_{air}-0.0025)^{1.6452}}{\phi_{air}}\right) & \text{for } \phi_{air} > 0.0025 \end{cases} \tag{26}$$

Fig. 19 shows that introducing only 0.25% of air decreases compressive strength by approximately 20%. This sharp decrease could hardly be measured experimentally since it compares a material without any defects such as macro-defect-free cements with a material with only a few voids or cracks. However, going to the region after this initial reduction yields a strength reduction of approx. 5% per 1% of entrained air, which is already consistent with the observation on the concrete scale [pp 557, 1].

4.5. Discussion on FE mesh representations

To demonstrate representativeness of a mesh, a cement paste from Level 2 was taken with the size 100 × 100 µm. Three sets of microstructures were generated using different mesh sizes, yielding 50 × 50, 100 × 100, and 200 × 200 quadrilateral elements. Five randomly generated microstructures in each set aimed at capturing statistical effect with 20% volume fraction of solid inclusions with stepwise particle size distribution using 5, 10, and 15 µm circular inclusions.

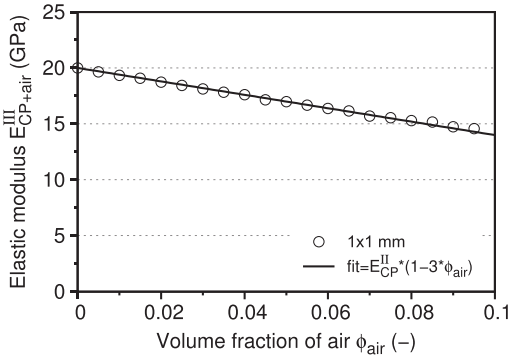

Fig. 17. Elastic modulus evolution for Level 3 (cement paste with air), assuming $E^{II}_{CP} = 20$ GPa. Circles represent results from FE simulations on a 2D microstructure on 50×50 quadrilateral elements (UC size 1×1 mm).

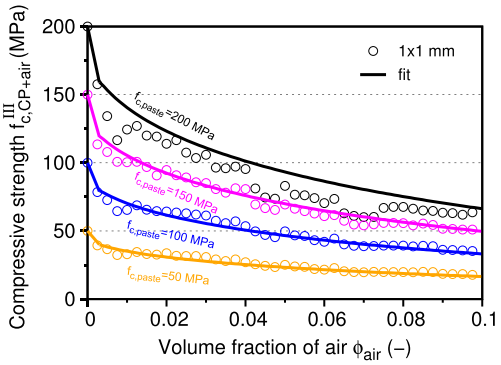

Fig. 18. Compressive strength evolution for Level 3 (cement paste with air). Circles represent results from FE simulations on a 2D microstructure on 50×50 quadrilateral elements (UC size 1×1 mm) for $f_{c^{II},CP}$ = 50, 100, 150, 200 MPa.

Simulations show that the predicted compressive strength of cement paste is almost insensitive to the mesh size, see Fig. 20. However, increasing mesh size results in a decrease of scatter in predicted compressive strengths, in accordance with theoretical predictions [42].

4.6. Calibration of $f_{t,glob}$

The proposed multiscale model contains two independent variables which need to be calibrated from experimental data

- The apparent tensile strength of C-S-H globules, $f_{t,glob}$.
- The spatial gradient of C-S-H described by the parameter β.

In this regard, we created the CemBase database version 1.0, containing experimental results from testing cement pastes and mortars. The data contained in this PostgreSQL database are structured and systematically sorted into individual categories starting from the characterization of raw materials, followed by the mixture composition, volume fractions of relevant phases, and measured mechanical properties. Individual categories are cross-linked to remove any duplicities.

Up to date, CemBase contains mechanical tests of 399 microstructures: 297 pastes and 102 mortars for water-to-binder ratios between 0.157 and 0.68. Complete volume fractions are not available for every microstructure due to missing experimental data. Whenever possible, the quantities of phases were calculated using a CEMHYD3D hydration model [41] to complement missing microstructural information.

Compressive strength is recorded for 353 microstructures between 1 and 750 days, however, our multiscale model was only validated against 95 paste compressive strength values as sufficient microstructural compositions are available here. Out of 95 strength values, 76 are from OPC

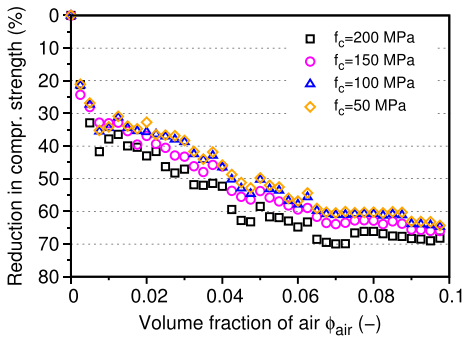

Fig. 19. Reduction of cement paste compressive strength with respect to entrapped or entrained air.

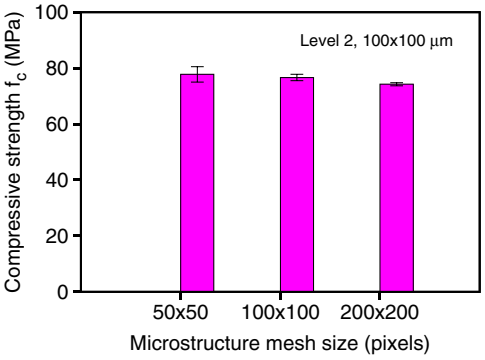

Fig. 20. Results from FE simulations on Level 2 (cement paste) containing 20% of solid inclusions for three mesh sizes.

pastes, 5 from slag-blended pastes, 5 from fly ash-blended pastes, 5 from limestone-blended pastes, and 4 from finely ground quartz-blended pastes. The volume of air is only recorded for 44 microstructures with an average value of 0.8%. The latter was assigned to the remaining microstructures as a default value.

During the calibration of our multiscale model, the parameter β was initially fixed to $\beta = 1$, which signalized a nearly uniform distribution of C-S-H in space as well as the highest possible compressive strength prediction. The apparent tensile strength for the C-S-H globule was identified using 95 experimental results of compressive strength as

$$f_{t,glob} = 320 \text{ MPa} \tag{27}$$

This strength is the highest value which is only exceeded by 6 out of 95 measured compressive strength values, see Fig. 21 (a). A further reduction of the model-predicted compressive strength is achieved by decreasing β, i. e. effectively by creating a gradient of C-S-H among cement grains. The value $\beta = 0.6$ globally fits the strength data best, however, the range $\beta \in \langle 0.4, 1 \rangle$ can accommodate almost all experimental results. Pastes from blended cements do not exhibit any substantial variations from the trend described by the C-S-H/space ratio, we, therefore, expect that the C-S-H formed from SCMs exhibits similar mechanical properties when compared to the C-S-H from pure OPC.

The theoretical tensile strength for cohesive brittle material is related to the E modulus through surface energy. Typical estimates are $f_t \in (0.01 - 0.10)E$ [43,44]. This gives a theoretical tensile strength of the C-S-H globule in the range $f_t \in (571 - 5710)$MPa which already shows high values on the small scale. Our apparent tensile strength for the C-S-H globule lies at the bottom range which already signalizes defects on this small scale.

Recently, tensile strength was measured indirectly on cantilever beams 20 µm long by means of bending [45]. The beams were prepared from 7 year old cement paste via FIB technique. Tensile strength of outer product (mainly C-S-H_{LD}) corresponded to 264.1 ± 73.4 MPa, inner product (mainly C-S-H_{HD}) 700.2 ± 198.5 MPa, while our model predicts values of 66 and 107 MPa, respectively. Such strength underestimation probably stems from oversimplified transition between levels 1 and 2. The homogenized C-S-H foam matrix on level 2 takes over uniform properties from level 1 while in reality C-S-H agglomerate dominantly around clinker grains. Such uneven distribution creates weaker links in the microstructure reducing its strength. Introducing random field for C-S-H foam's tensile strength offers a solution how to calibrate multiscale model for matching C-S-H experimental tensile strength. This clearly demonstrates increase of strength with size decrease and supports the high tensile strength of C-S-H globule.

The formation of the C-S-H gradient inevitably leads to a decrease of compressive strength. A possible way of interpreting the C-S-H gradient is that as C-S-H precipitates on clinker grains it starts to

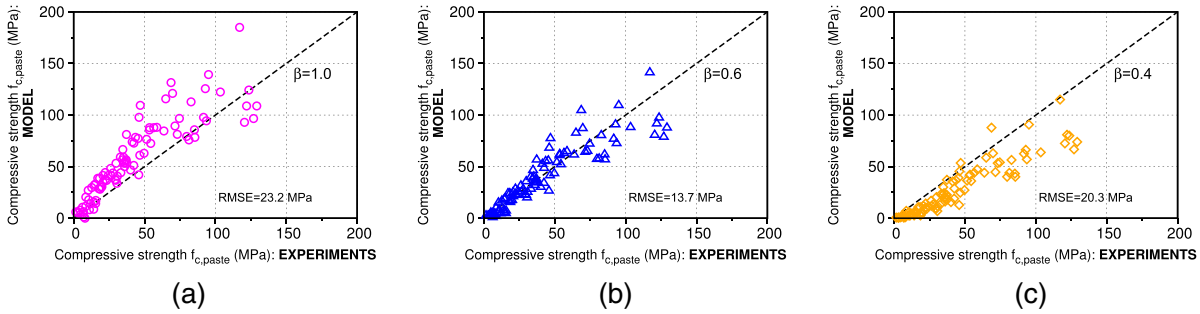

Fig. 21. Validation of model-predicted compressive strength with experiments for $\beta = 1.0$ (a), $\beta = 0.6$ (b), and $\beta = 0.4$ (c).

grow onwards, filling capillary porosity. For cement pastes with a relatively high w/b ratio clinker grains are widely spaced apart from each other, C-S-H fail to interconnect neighbouring grains to create a solid structural network. Densifying the microstructure, either by lowering w/b ratio, by providing additional mineral surfaces for C-S-H to precipitate onto or by filling capillary porosity by a fine material (such as silica fume), inevitably leads to a more dispersed C-S-H precipitation. This results in a low gradient of C-S-H (described by a high parameter β) and corresponds to high strength predictions, see Fig. 22 (a) for pastes with $w/b \leq 0.4$. Pastes with a higher water-to-binder ratio ($w/b > 0.4$) tend to exhibit a larger gradient of C-S-H (described by a low parameter β) due to a less dense packing of clinker grains, see Fig. 22 (b).

The scaling parameter β takes into account several factors, notably heterogeneous nucleation and precipitation of C-S-H and cement fineness. These factors are normally overlooked since calibration data usually come from similar cements without seeding agents or with various blend levels. Recognizing this effect opens a way to optimize distribution of C-S-H and to improve a binder.

4.7. Validation of elastic modulus

The elastic modulus of cement paste was validated against 27 experimental results from CemBase. The validation assumed $\beta = 1.0$ and $\beta = 0.6$ for all experimental results, see Fig. 23. Lower values of β lead to slightly lower model predictions.

4.8. Example #1 - Portland cement paste w/c = 0.51

This example illustrates the performance of the multiscale model on OPC with $w/b = 0.51$. The microstructural characterization in Fig. 24 (a) was performed at 3, 7, 28, and 91 days at Lafarge Centre de Recherche according to the test protocol described in [10] using a combination of XRD/Rietveld together with thermal gravimetric analysis and volume balance equations and provides the necessary volume fractions for the model. A high water-to-binder ratio creates a sparsely filled microstructure which, at the same time, results in a high gradient of C-S-H.

Fig. 24 (b) shows a validation where a low parameter $\beta = 0.6$ fits the best experimental results. The last experimental strength value measured at 91 days shows no increase when compared to 28 days. In this particular case the specimen had dried out, which is further supported by mass measurements taken directly after demoulding of the specimen and before testing. The specimen was kept for 91 days in a cooling chamber with 95% RH, 20 °C and was wrapped in a food-preservation plastic foil to further reduce water evaporation. However, such precautions were insufficient and surface microcracks were very likely formed which resulted in a lower-than-expected compressive strength. Table 2 shows a decrease of model-predicted tensile and compressive strength with upscaling.

4.9. Example #2—Portland cement paste w/c = 0.247

To study the impact of the water-to-binder ratio on observed mechanical properties, we extract a substoichiometric cement paste with $w/b = 0.247$ from CemBase. Volume fractions were calculated by CEMHYD3D hydration model [41] using raw material characterization found in [46]. The necessary input for the multiscale model comes from the volume fraction in Fig. 25 (a). A relatively low $w/b = 0.247$ indicates a dense microstructure, forcing C-S-H to evenly precipitate within capillary pores. This is best described by $\beta = 0.8$, see Fig. 25 (b). Table 3 shows a decrease of model-predicted tensile and compressive strength with upscaling.

4.10. Example #3—slag-blended cement paste w/b = 0.53

The results from a microstructural characterization carried out on a slag-blended paste with $w/b = 0.53$ by mass ($w/b = 1.6$ by volume),

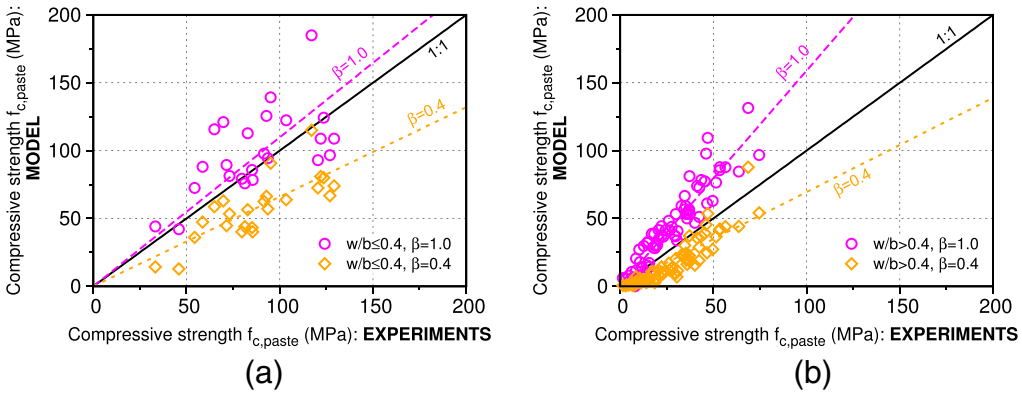

Fig. 22. Impact of the water-to-binder ratio on the C-S-H gradient, represented by the parameter β: (a) dense microstructures with $w/b \leq 0.4$ exhibit a more uniform C-S-H formation signalized by $\beta = 1$, whereas (b) sparse microstructures with $w/b > 0.4$ indicate a higher C-S-H gradient.

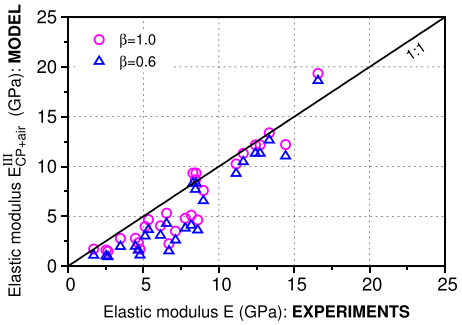

Fig. 23. Model predicted elastic modulus for $\beta=1.0$ and $\beta=0.6$.

the 45% cement replacement level are shown in Fig. 26 (a). The characterization of individual chemical phases was performed at 1, 3, 7, 28, and 91 days in the same way as in Section 4.8. The model-predicted compressive strength is shown in Fig. 26 (b). The most appropriate value is $\beta=0.5$.

4.11. Example #4—fly ash-blended cement paste w/b = 0.60

The results from a microstructural characterization carried out on a fly ash-blended paste with $w/b=0.60$ by mass ($w/b=1.6$ by volume), the 45% cement replacement level are shown in Fig. 27 (a). The characterization of individual chemical phases was performed at 1, 3, 7, 28, and 91 days in the same way as in Section 4.8 . The model-predicted compressive strength is shown in Fig. 27 (b). The most appropriate value is $\beta=0.5$.

4.12. Comparison with Powers' approach

Direct comparison of Powers' gel/space model [47] and the presented model is not straightforward because both are based on different microstructural descriptors. However, we will show that under some reasonable assumptions both approaches yield comparable results. Powers coined an empirical relation between the microstructure of pure cement pastes and their compressive strength using "gel/space" ratio (GSR) as a microstructural descriptor. This relation can be expressed by a power law function as

$$f_{c,paste} = f_0\ \mathrm{GSR}^b \tag{28}$$

where f_0 stands for the intrinsic compressive strength of the material and b for the best fit coefficient. Similar power law function can also be identified when the microstructure is described by "C-S-H/space" ratio, γ_{CSH}, see Fig. 28.

Table 2
Decrease of strength with upscaling for OPC paste, $w/b=0.51$ at 28 days (degree of OPC hydration $\xi=0.836$) using microstructural characterisation as follows: $\gamma_{CSH}=0.60742$, $f_{cappor}=0.290$, $f_{incl}=0.2381$, $E_{incl}=48.032$ GPa, $f_{air}=0.008$, $\beta=0.6$, and $f_{t,glob}=320$ MPa.

	Level 0 C–S–H	Level 1 C–S–H foam	Level 2 Cement paste	Level 3 Cement paste with air	
f_t^i	68.754	8.592	6.515	4.730	MPa
f_c^i	550.029	68.738	52.119	37.835	MPa

The presented multiscale model uses four hierarchical levels to describe the microstructure. To simplify the strength prediction into a single equation, we make the following assumptions: (i) at Level 0 we assume the ratio of C-S-H $_{LD}$:C-S-H $_{HD}$ equal to 4:1; (ii) at Level 1 the spatial gradient of C-S-H by $\beta=0.6$; (iii) at Level 2 the volume fraction of inclusions equals to 0.15; and (iv) at Level 3 the volume of entrained air equals to 0.008. The expression of compressive strength of then simplifies into a single exponential equation

$$f_{c,paste} = 320\exp\left(-1.3412\frac{1-\gamma_{CSH}{}^{5.7072}}{\gamma_{CSH}}\right) \tag{29}$$

Fig. 28 shows the comparison of both approaches with very similar results. However, varying the scaling parameter β results in upper and lower bounds that can cover almost all experimental data points.

4.13. Impact of C-S-H fracture energy

It is an interesting feature of the four-level model that compressive or tensile strength always decreases on upscaling. Fracture energy may increase on upscaling if other mechanisms occur during the crack propagation, e.g. crack arresting, shielding, or pulling out an inclusion. It is also known from concrete experiments that fracture energy increases with the size of aggregates [48].

A direct experimental characterization of fracture energy for C-S-H is currently, up to our best knowledge, beyond experimental evidence. C-S-H as an amorphous precipitate contains micro-crystalline seeds of CH and other crystalline hydration products (AFm, AFt) which increase the observed fracture energy. Modeling of frictional pull-out tests [25] of CH from the C-S-H matrix tend to increase the fracture energy due to intermolecular interactions between C-S-H globules.

Numerical modeling on Level 1, see Fig. 29, shows that the fracture energy of C-S-H only has an insignificant impact on the predicted compressive strength. Decreasing $G^0_{f,CSH}$ below 2 J/m^2 would increase the apparent tensile strength of a globule, $f_{t,glob}$, [25].

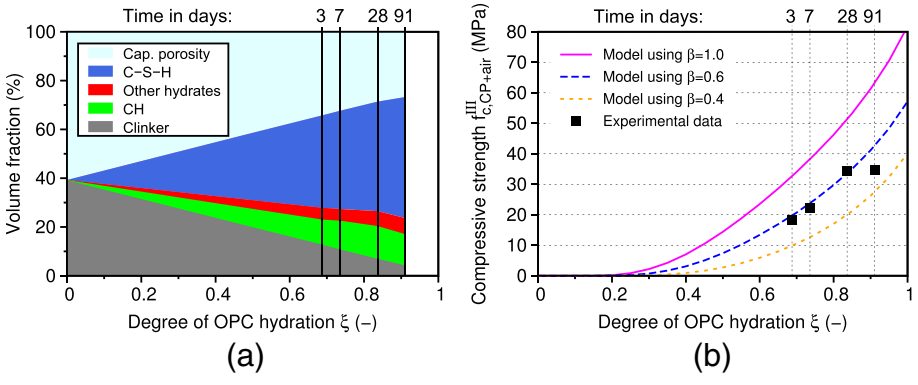

Fig. 24. Volume fractions for OPC paste with $w/b=0.51$ (a). Experimentally measured compressive strength (b) compared with multiscale model predictions.

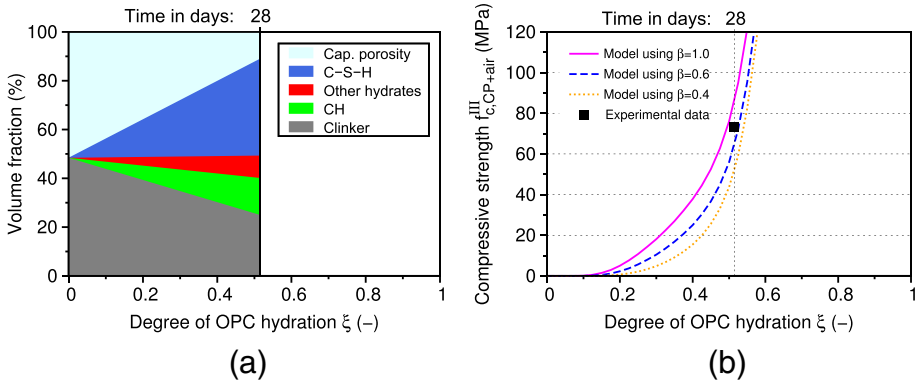

Fig. 25. Volume fractions for OPC paste with $w/b = 0.247$ (a). Experimentally measured compressive strength (b) compared to model predictions.

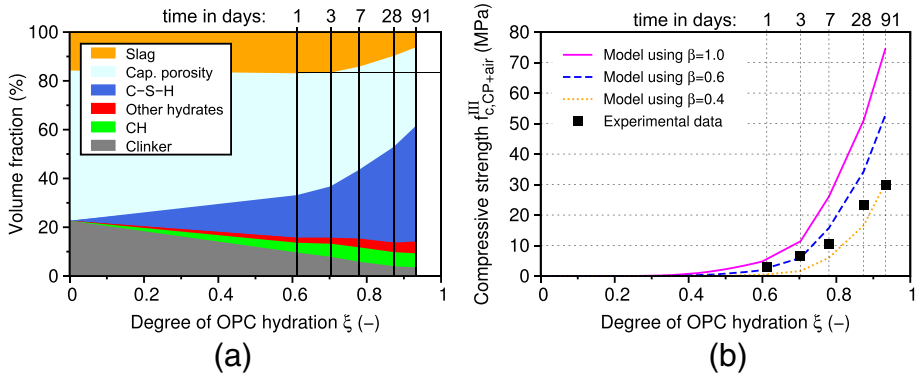

Fig. 26. Volume fractions for slag-blended paste with $w/b = 0.53$ and the replacement level of 45% by volume (a). Experimentally measured compressive strength (b) compared to model predictions.

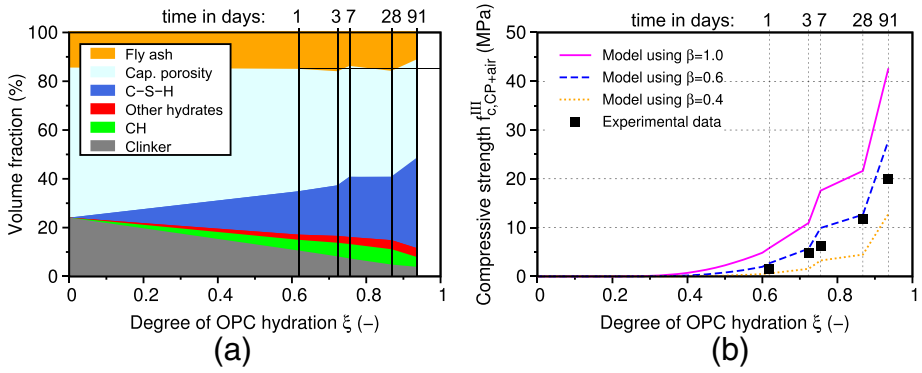

Fig. 27. Volume fractions for fly ash-blended paste with $w/b = 0.60$ and the replacement level of 45% by volume (a). Experimentally measured compressive strength (b) compared to model predictions

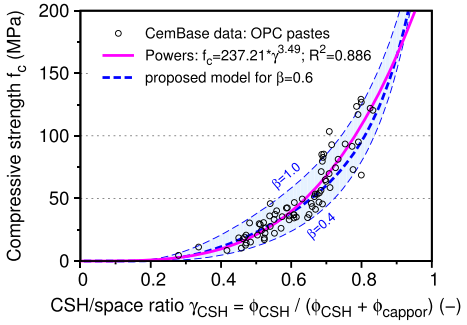

Fig. 28. Comparison of modeling approaches: Powers' power law fit and proposed model.

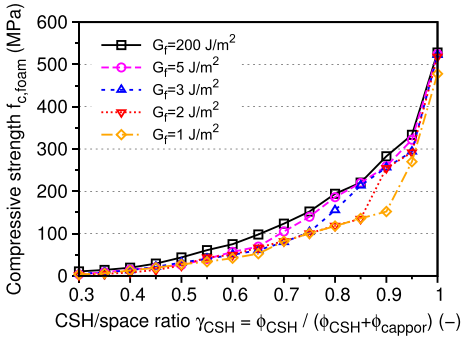

Fig. 29. Impact of fracture energy of C-S-H on compressive strength of C-S-H foam. FE model from 10×10×20 brick elements (UC size 5×5×10 μm) using $\beta = 1.0$.

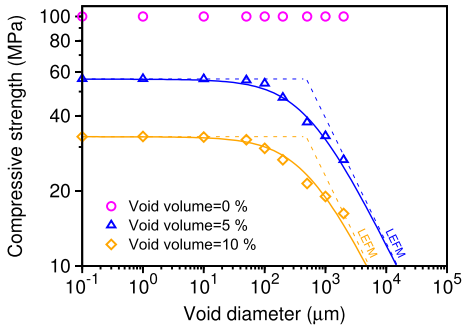

Fig. 30. Void size-dependent compressive strength of cement paste obeying the size-effect law.

4.14. Impact of void size on strength

Voids in cement paste occur on different length scales either as capillary pores (size 10 nm − 10 μm) or as entrained air (10 μm − 500 μm) or entrapped air (>1 mm). In quasi-brittle materials the size of voids matters as the scaling of compressive (tensile) strength obeys the size-effect law [17]

$$\sigma_{N,c} = B f_c' \left(1 + \frac{d}{d_0}\right)^{-\frac{1}{2}} \tag{30}$$

where d is the void diameter, d_0, B, f_c' are constants for identification. In a perfectly ductile material, the diameter of a void does not matter. The level of C-S-H foam resembles this situation with the size up to 10 μm, see Fig. 12, which renders the foam less brittle with larger softening part. Capillary pores residing in the foam influence strength by their volume only, while the shape and their distribution have a little influence. This is the reason why the total amount of capillary porosity controls compressive/tensile strength, but neither their pore distribution nor their shape.

The situation changes for entrapped/entrained air voids which have a much larger size than capillary voids. In a perfectly brittle material, increasing a void size four-times would decrease the strength twice according to linear elastic fracture mechanics. Also, the shape of void influences the strength of material. Cement paste is a quasibrittle material hence the scaling of strength occurs between ductile and brittle asymptotic limits.

Fig. 30 shows results from a size effect study on a 2D microstructure (100×100 quadrilateral elements). The model is not directly associated to any homogenization level in particular, see Fig. 5, but covers the whole range of sizes. The model consists of a homogeneous matrix ($f_c = 100$ MPa and $G_f = 15$ J/m^2) with voids. The actual void diameter is kept constant at 10 elements whereas the volume fraction changes from 0 up to 10%. Changing the element resolution creates different sizes of the identical microstructure, starting from 1×1 μm with void size 0.1 μm up to 2×2 cm with void size 2 mm. It is clear that void diameters $d>50$ μm reduce the strength more than only by their volume amount. This is due to a more brittle behavior of the cement paste than the foam. The presence of entrapped air with $d>1$ mm is the most detrimental.

Table 3
Decrease of strength with upscaling for OPC paste, $w/b = 0.247$ at 28 days (degree of OPC hydration $\xi = 0.515$) using microstructural characterisation as follows: $\gamma_{CSH} = 0.77564$, $f_{cappor} = 0.1146$, $f_{incl} = 0.4892$, $E_{incl} = 79.033$ GPa, $f_{air} = 0.041$, $\beta = 0.8$, and $f_{t,glob} = 320$ MPa.

	Level 0 C–S–H	Level 1 C–S–H foam	Level 2 Cement paste	Level 3 Cement paste with air	
f_t^i	79.673	24.404	18.498	9.289	MPa
f_c^i	637.381	195.231	147.985	74.311	MPa

4.15. Global sensitivity analysis by scatter plots

Sensitivity analysis by a sampling-based method identifies the key global factors influencing compressive/tensile strength. Compressive strength is calculated using a full factorial design from a combination of all input variables on each scale. Model inputs for each level were chosen by uniform sampling over all admissible model input as follows:

- C-S-H/space ratio $\gamma_{CSH} \in \langle 0.3, 1 \rangle$ for Level 1.
- Volume fraction of C-S-H $_{HD}$within C-S-H:$\phi_{CSH_{HD}} \in \langle 0, 1 \rangle$ for Level 1.
- Parameter for C-S-H spatial gradient: $\beta \in \langle 0.4, 1 \rangle$ for Level 1.
- Volume fraction of inclusion: $\phi_{incl} \in \langle 0, 1 \rangle$ for Level 2.
- Volume fraction of entrapped/entrained air:$\phi_{air} \in \langle 0, 0.1 \rangle$ for Level 3.

Compressive strength is plotted against a combination of individual input variables in a scatter plot which provides a visual indication of the sensitivity of a given input value. Spearman's rank correlation coefficient ρ is used to quantify sensitivity; the closer the $|\rho|$ is to 1, the more monotonically related the observed variables are.

Input variables on all levels cover a wide range of possible combinations of admissible data for the multiscale model. Fig. 31 shows the most correlated input variables globally; the C-S-H/space ratio and the volume fraction of entrapped/entrained air.

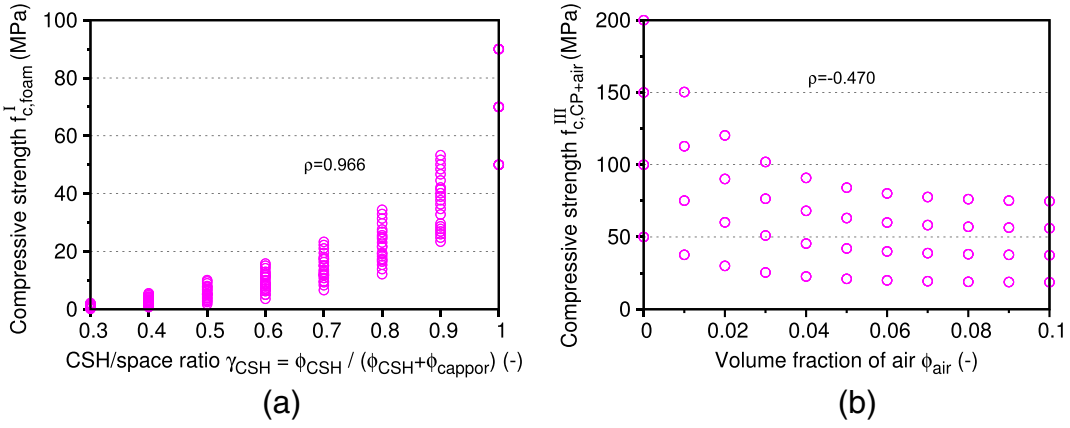

Fig. 31. Important results from global sensitivity analysis; (a) correlation between the compressive strength of C-S-H foam and the C-S-H/space ratio, and (b) compressive strength of cement paste and volume fraction of air.

Table 4
Local sensitivity analysis on OPC paste, $w/c = 0.51$ at 28 days.

Model input X_i	Default value **X**	Impact on compressive strength $\frac{\partial f_{c,CP+air}^{III}}{\partial X_i}\|_{\mathbf{X}}$
Air volume fraction ϕ_{air}	0.008	−491.67
C-S-H/space ratio γ_{CSH}	0.608	181.85
Spatial gradient of C-S-H β	0.600	58.37
C-S-H $_{HD}$ volume fraction $\phi_{CSH_{HD}}$	0.094	19.16
Inclusion volume fraction ϕ_{incl}	0.267	−0.15
Elastic modulus of inclusion E_{incl} (GPa)	48.032	0.00

4.16. Local sensitivity analysis

To further highlight the impact of individual input parameters on model predictions, local sensitivity analysis was carried out for selected cement pastes. Local sensitivity analysis considers the effect of small perturbations of one model input variable (X_i) to the compressive strength while keeping the other inputs constant (**X**)

$$\frac{\partial Y}{\partial X_i}\Big|_{\mathbf{X}} \tag{31}$$

The partial derivative in Eq. (31) is solved using a forward difference method with the step length equal to 1 % of the input value. The higher the absolute value of the partial derivation, the more sensitive the input parameter. However, the step length is kept equal for assessment of all input variables, disregarding the actual range for the input parameter. This results in unequal model predictions because changing the volume fraction of air by 1 % (with a range from 0 to 0.1) reduces predicted compressive strength significantly more than changing, e.g. β by 1 % (with a range from 0.4 to 1). Therefore the presented local sensitivity analysis only shows trends and highlights key microstructural factors rather than comparing absolute values of the partial derivation.

Local sensitivity analysis was performed on all mixes in four examples (OPC with $w/b = 0.51$, OPC with $w/b = 0.247$, slag-blended paste with 45% clinker replacement, and fly ash-blended paste with 45% clinker replacement). The results were very similar and only the OPC paste $w/b = 0.51$ is shown in Table 4. Results highlighted that apart from the C-S-H/space ratio and entrapped air, the spatial gradient of C-S-H plays a key role for the compressive strength and elastic modulus of cement paste.

5. Conclusions

The paper describes a four-level micromechanical model for blended cement pastes aimed at predicting compressive strength. The multiscale model uses a newly-proposed "C-S-H/space" ratio as the primary microstructural descriptor which is applicable for pure as well as blended cements. The model introduces a spatial C-S-H gradient, mimicking nonuniform distribution between individual grains. The most relevant findings and conclusions can be summarized as follows:

1. The C-S-H globule was taken as the only failing phase which obeys an elasto-damage law with linear softening. Other chemical phases were treated elastically. Validation proved that this assumption can cover all experimental data on OPC and blended pastes with the addition of slag, fly ash, limestone and quartz and w/b in the range of 0.157 up to 0.68 from approximately 1 day of hydration under room temperature.
2. The CemBase database version 1.0 was assembled for validating the multiscale model. The database now contains 399 experimental data.
3. The apparent tensile strength of the C-S-H globule was identified as $f_{t,glob} = 320$ MPa by evaluating the model predicted compressive strength against 95 experimental values. Although there is no direct experimental evidence of such high tensile strength, the theoretical limit value can be as high as 5700 MPa [43,44]. More experimental and bottom-up evidence is needed for calibrating this apparent tensile strength.
4. The C-S-H/space ratio was found to be the most fundamental parameter for compressive/tensile strength, in accordance with Powers [30]. The volume of entrained/entrapped air and the spatial gradient of C-S-H are further factors governing the compressive strength of blended pastes.
5. Precipitating C-S-H around grains exhibit a spatial gradient which has a strong impact on the compressive strength of cement paste. The densification of the microstructure due to a decrease of the initial water-to-binder ratio or by progressing hydration leads to a more uniform distribution of C-S-H. This assumption was proved by true μCT using two-point correlation functions.
6. The multiscale model needs further elaboration for systems beyond the OPC basis producing C-S-H. Particularly alkali-activated systems (N-A-S-H gel), calcium aluminate cements (C-A-H gel), oxychloride, phosphatic cements, etc.
7. The multiscale model captures the strain-softening behavior on each scale and handles energy dissipation by upscaling E, f_t and assigning G_f. This ensures a correct localization limiter on each scale and the transfer of microstructurally-based fracture properties between scales [49].

Acknowledgment

The authors gratefully acknowledge "NANOCEM" funding within Core Project 10 "Micromechanical Analysis of Blended Cement-Based Composites" and support from CTU grant SGS15/030/OHK1/1T/11 and from Czech Science Foundation 16-20008S. We appreciate stimulating discussions on NANOCEM events, particularly contributions from Bernhard Pichler (TU Wien) and Klaus-Alexander Rieder (WR Grace). NANOCEM's funding further allowed Michal Hlobil's internship in Lafarge Centre de Recherche during 2012–2013.

The authors would like to pay tribute to Gilles Chanvillard, who passed away on Oct 24, 2015. Here, Gilles contributed significantly to microstructural and mechanical understanding of cementitious composites, built several bridges between industrial and academic environment and his cheerful spirit helped to enjoy research and science.

References

[1] A.M. Neville, Properties of Concrete, John Wiley & Sons, Inc., 1997
[2] The Cement Sustainability Initiative, 10 Years of Progress and Moving on into the Next Decade, 2012.
[3] E. Gartner, Industrially interesting approaches to "low-CO2" cements, Cem. Concr. Res. 34 (9) (2004) 1489–1498, http://dx.doi.org/10.1016/j.cemconres.2004.01.021.
[4] E.M. Gartner, D.E. Macphee, A physico-chemical basis for novel cementitious binders, Cem. Concr. Res. 41 (7) (2011) 736–749.
[5] L. Lam, Y. Wong, C. Poon, Degree of hydration and gel/space ratio of high-volume fly ash/cement systems, Cem. Concr. Res. 30 (5) (2000) 747–756, http://dx.doi.org/10.1016/S0008-8846(00)00213-1.
[6] B. Pichler, C. Hellmich, Upscaling quasi-brittle strength of cement paste and mortar: a multi-scale engineering mechanics model, Cem. Concr. Res. 41 (5) (2011) 467–476, http://dx.doi.org/10.1016/j.cemconres.2011.01.010.
[7] B. Pichler, C. Hellmich, J. Eberhardsteiner, J. Wasserbauer, P. Termkhajornkit, R. Barbarulo, G. Chanvillard, Effect of gel–space ratio and microstructure on strength of hydrating cementitious materials: an engineering micromechanics approach, Cem. Concr. Res. 45 (0) (2013) 55–68.
[8] V. Nežerka, J. Zeman, A micromechanics-based model for stiffness and strength estimation of cocciopesto mortars, Acta Polytech. 52 (6) (2012) 29–37.
[9] B. Pichler, S. Scheiner, C. Hellmich, From micron-sized needle-shaped hydrates to meter-sized shotcrete tunnel shells: micromechanical upscaling of stiffness and strength of hydrating shotcrete, Acta Geotech. 3 (4) (2008) 273–294.
[10] P. Termkhajornkit, Q.H. Vu, R. Barbarulo, S. Daronnat, G. Chanvillard, Dependence of compressive strength on phase assemblage in cement pastes: Beyond gel–space ratio — Experimental evidence and micromechanical modeling, Cem. Concr. Res. 56 (0) (2014) 1–11, http://dx.doi.org/10.1016/j.cemconres.2013.10.007.
[11] F. Ganneau, F.-J. Ulm, J. Gondzio, E. Garboczi, An algorithm for computing the compressive strength of heterogeneous cohesive-frictional materials—application to cement paste, computers and geotechnics, Chemo Mech. Interact. Geomater. 34 (4) (2007) 254–266, http://dx.doi.org/10.1016/j.compgeo.2007.02.005.

[12] G. Cusatis, Z.P. Bažant, L. Cedolin, Confinement-shear lattice model for concrete damage in tension and compression: II. Computation and validation, J. Eng. Mech. 129 (12) (2003) 1449–1458.
[13] P. Grassl, M. Jirásek, Meso-scale approach to modelling the fracture process zone of concrete subjected to uniaxial tension, Int. J. Solids Struct. 47 (7–8) (2010) 957–968, http://dx.doi.org/10.1016/j.ijsolstr.2009.12.010.
[14] S.-M. Kim, R.K.A. Al-Rub, Meso-scale computational modeling of the plastic-damage response of cementitious composites, Cem. Concr. Res. 41 (3) (2011) 339–358.
[15] H.M. Jennings, Refinements to colloid model of C-S-H in cement: CM-II, Cem. Concr. Res. 38 (3) (2008) 275–289.
[16] M. Jirásek, S. Rolshoven, Localization properties of strain-softening gradient plasticity models. Part I: Strain-gradient theories, Int. J. Solids Struct.0 46 (11–12) (2009) 2225–2238, http://dx.doi.org/10.1016/j.ijsolstr.2008.12.016.
[17] Z.P. Bažant, J. Planas, Fracture and Size Effect in Concrete and Other Quasibrittle Materials, CRC Press, 1998.
[18] A. Griffith, Theory of rupture, in: C. Biezeno, J. Burgers (Eds.),First International Congress for Applied Mechanics, Delft 1924, pp. 55–63.
[19] F. McClintock, J. Walsh, Friction of Griffith cracks in rock under pressure, Proc. Fourth U.S. National Congress of Applied Mechanics, New York City 1962, pp. 1015–1021.
[20] M. Jirásek, Z.P. Bažant, Inelastic Analysis of Structures, John Wiley & Sons, Ltd., 2002
[21] B. Patzák, et al., Object Oriented Finite Element Method—OOFEM, http://www.oofem.org (since 1993.
[22] Z.P. Bažant, Y. Xiang, Size effect in compression fracture: splitting crack band propagation, J. Eng. Mech. 123 (2) (1997) 162–172.
[23] V. Šmilauer, Z. Bittnar, Microstructure-based micromechanical prediction of elastic properties in hydrating cement paste, Cem. Concr. Res. 36 (9) (2006) 1708–1718.
[24] O. Bernard, F.-J. Ulm, E. Lemarchand, A multiscale micromechanics-hydration model for the early-age elastic properties of cement-based materials, Cem. Concr. Res. 33 (9) (2003) 1293–1309.
[25] T.T. Ghebrab, P. Soroushian, Mechanical properties of hydrated cement paste: development of structure–property relationships, Int. J. Concr. Struct. Mater. 41 (1) (2010) 37–43.
[26] M. Bauchy, H. Laubie, M.A. Qomi, C. Hoover, F.-J. Ulm, R.-M. Pellenq, Fracture toughness of calcium-silicate-hydrate from molecular dynamics simulations, J. Non-Cryst. Solids 419 (0) (2015) 58–64, http://dx.doi.org/10.1016/j.jnoncrysol.2015.03.031 URL http://www.sciencedirect.com/science/article/pii/S0022309315001362.
[27] G. Constantinides, F.-J. Ulm, The effect of two types of C-S-H on the elasticity of cement-based materials: results from nanoindentation and micromechanical modeling, Cem. Concr. Res. 34 (1) (2004) 67–80.
[28] C.-J. Haecker, E.J. Garboczi, J.W. Bullard, R.B. Bohn, Z. Sun, S.P. Shah, T. Voigt, Modeling the linear elastic properties of Portland cement paste, Cem. Concr. Research 35 (10) (2005) 1948–1960.
[29] V. Šmilauer, P. Hlaváček, P. Padevět, Micromechanical analysis of cement paste with carbon nanotubes, Acta Polytech. 52 (1998) 35–41.
[30] T.C. Powers, T.L. Brownyards, Studies of physical properties of hardened portland cement paste, Bulletin 22, Research Laboratories of the Portland Cement Association, Chicago, March 1948.
[31] G.W. Scherer, Structure and properties of gels, Cem. Concr. Res. 29 (8) (1999) 1149–1157, http://dx.doi.org/10.1016/S0008-8846(99)00003-4.
[32] D.P. Bentz, S. Mizell, S. Satterfield, J. Devaney, W. George, P. Ketcham, J. Graham, J. Porterfield, The visible cement data set, J. Res. Natl. Inst. Stand. Technol. 107 (2) (2002) 137–148http://visiblecement.nist.gov.
[33] K. van Breugel, Numerical simulation of hydration and microstructural development in hardening cement-based materials, Cem. Concr. Res. 25 (2) (1995) 319–331.
[34] A. Princigallo, P. Lura, K. van Breugel, G. Levita, Early development of properties in a cement paste: a numerical and experimental study, Cem. Concr. Res. 33 (7) (2003) 1013–1020.
[35] S. Bishnoi, K.L. Scrivener, uic: A new platform for modelling the hydration of cements, Cem. Concr. Res. 39 (4) (2009) 266–274, http://dx.doi.org/10.1016/j.cemconres.2008.12.002 URL http://www.sciencedirect.com/science/article/pii/S0008884608002214.
[36] S. Bishnoi, K.L. Scrivener, Studying nucleation and growth kinetics of alite hydration using uic, Cem. Concr. Res. 39 (10) (2009) 849–860, http://dx.doi.org/10.1016/j.cemconres.2009.07.004 URL http://www.sciencedirect.com/science/article/pii/S0008884609001641.
[37] J. Beaudoin, V. Ramachandran, A new perspective on the hydration characteristics of cement phases, Cem. Concr. Res. 22 (4) (1992) 689–694, http://dx.doi.org/10.1016/0008-8846(92)90021-M.
[38] A.V. Hershey, The elasticity of an isotropic aggregate of anisotropic cubic crystals, J. Appl. Mech. 21 (3) (1954) 236–240.
[39] H.M. Jennings, A model for the microstructure of calcium silicate hydrate in cement paste, Cem. Concr. Res. 30 (6) (2000) 101–116.
[40] G. Constantinides, F.-J. Ulm, The nanogranular nature of C-S-H, J. Mech. Phys. Solids 55 (2007) 64–90.
[41] D.P. Bentz, CEMHYD3D: A Three-Dimensional Cement Hydration and Microstructure Development Modeling Package. Version 3.0. Tech. rep., NIST Building and Fire Research Laboratory, Gaithersburg, Maryland, 2005.
[42] T. Kanit, S. Forest, I. Galliet, V. Mounoury, D. Jeulin, Determination of the size of the representative volume element for random composites: statistical and numerical approach, Int. J. Solids Struct. 40 (2003) 3647–3679.
[43] D.K. Felbeck, A.G. Atkins, Strength and Fracture of Engineering Solids, Prentice-Hall, New Jersey, 1984.
[44] H. Gao, Application of fracture mechanics concepts to hierarchical biomechanics of bone and bone-like materials, Int. J. Fract. 138 (1-4) (2006) 101–137.
[45] J. Němeček, V. Králík, V. Šmilauer, L. Polívka, A. Jäger, Tensile strength of hydrated cement paste phases assessed by micro-bending tests and nanoindentation, Cem. Concr. Compos. (2015) *submitted*.
[46] J.-M. Mechling, A. Lecomte, C. Diliberto, Relation between cement composition and compressive strength of pure pastes, Cem. Concr. Compos. 31 (4) (2009) 255–262, http://dx.doi.org/10.1016/j.cemconcomp.2009.02.009.
[47] T.C. Powers, Structure and physical properties of hardened Portland cement paste, J. Am. Ceram. Soc. 41 (1) (1958) 1–6.
[48] F.H. Wittmann, Crack formation and fracture energy of normal and high strength concrete, Sadhana 27 (4) (2002) 413–423.
[49] Z.P. Bažant, Can multiscale-multiphysics methods predict softening damage and structural failure? Int. J. Multiscale Comput. Eng. 8 (1) (2010) 61–67.